Surface & Coatings Technology 466 (2023) 129638

Contents lists available at ScienceDirect

Surface & Coatings Technology

journal homepage: www.elsevier.com/locate/surfcoat

High-velocity laser accelerated deposition (HVLAD): An experimental study

Keivan Davami [a,*,1], Majid Vaseghi [a,1], Nicholas Brooks [a,1], Russell Rowe [a], Noah Holtham [a], Trevor Southers [a], Taejeong Um [a], Lloyd Hackel [b]

[a] Department of Mechanical Engineering, University of Alabama, Tuscaloosa, AL 35487, USA
[b] Curtiss Wright Surface Technologies, Metal Improvement Company, Livermore, CA, 94551, USA

ARTICLE INFO

Keywords:
High-velocity laser accelerated deposition
Laser peening
Microstructural characterization
Mechanical characterization
Surface engineering

ABSTRACT

A versatile solid-state cladding technique named high-velocity laser accelerated deposition (HVLAD), which is capable of creating highly uniform coverage on various surfaces, is reported here. The method is a non-thermally driven, mechanically based process that relies on laser peening (LP) technology which has been used for commercial applications for decades. In HVLAD, a high-intensity laser is used to accelerate, propel, and deposit small areas of a thin film in a controlled step-by-step manner onto a substrate. This process can be repeated until a desired thickness of material is deposited onto the substrate. This technique does not generate any large variations in temperature between the thin film and the substrate material. Instead, it employs intense laser pulses with energies up to 50 J for a duration of 8–50 ns to create a plasma generated pressure wave which accelerates the thin film in the order of a few hundred meters per second into the substrate material. Two cladding methods were evaluated in this study including the confined method, which incorporates a confining water media and a vinyl tape overlay, and the unconfined method which does not. High speed and thermal imaging cameras showed no macrolevel melting or significant temperature increase in the clad or substrate material during the cladding process, however signs of microlevel melting and re-solidification were observed at the interface primarily in specimens cladded using the unconfined method. Grain structures in adjacent areas to the clad location remained preserved using both methods, and no signs of any phase or alloy composition changes, except for at the interface, were observed. The effects of a confining media (water) and vinyl tape in the process were studied both analytically and experimentally and a change in the deposition mechanism was observed. With further research and development this technique has the ability to be used to deposit a variety of coatings without any limitations dictated by their strength on complex geometries in a cost-effective manner. The HVLAD process can be implemented to deposit corrosion, wear, thermal, and even impact-resistant coatings with strong bonding on a wide range of substrates.

1. Introduction

There is a significant need for the development of novel techniques for joining dissimilar materials. In this regard, solid-state joining processes are of interest, not only because a smaller quantity of defects are formed due to the absence of the liquid phase during the process and low heat input conditions, but also since solid-state processes do not have common drawbacks of many other joining techniques [1,2]. Residual stresses that cause expansion or distortion of the structure, localized changes in the hardness, formation of a heat affected zone, solidification cracking, and creation of anisotropic mechanical properties that are relatively common in fusion-based joining processes are not an issue in solid-state processes [3–8]. Also, there is no need for a subsequent heat treatment to release the residual stresses that might affect the functionality of the structure or considerations for the difference in the melting points or thermal expansion coefficients of the joining materials that are major drawbacks in fusion-based processes [9,10]. Another advantage of solid-state joining processes is that non-ferrous alloys which are challenging to join using fusion welding, can be joined readily by implementing solid-state techniques and without the need for a filler material. The contact interface between the parts in fusion-based welding operations is typically composed of seams or even sparse spots, while in many solid-state processes, the entire contact interface between the two parts is the welded joint [2].

* Corresponding author.
E-mail address: kdavami@eng.ua.edu (K. Davami).
[1] These authors contributed equally.

https://doi.org/10.1016/j.surfcoat.2023.129638
Received 6 February 2023; Received in revised form 2 May 2023; Accepted 12 May 2023
Available online 18 May 2023

A wide range of cladding and coating techniques have been developed and implemented in recent years such as flame spray, plasma spray, high-velocity oxy-fuel (HVOF) deposition, and cold spray [11–14]. However, many of these techniques suffer from disadvantages such as relatively weak interfacial bonds, and voids that develop during the processes. Additionally, in many of these techniques, such as chemical vapor deposition (CVD) and physical vapor deposition (PVD), delamination of the coating material occurs which worsens with an increase in the thickness of the coating material [15]. While these techniques can produce coatings with a relatively narrow range of elemental compositions, other challenges such as the surface roughness of the coating, which is amplified due to low mass flux in CVD and PVD, still need to be addressed.

The demand for dissimilar material joining processes across various industries, in addition to the deficiencies in current material joining techniques, emphasizes the need for the development of solid-state joining processes. In such processes there are fewer defects in the joined material due to the absence of the liquid phase. The difference in the melting points of the materials is not an issue, and other thermal related issues such as thermal expansion and warping, which are common in diffusion-based techniques, are not of concern.

Laser-based deposition technologies are widely used, and new methods are emerging at an unprecedented rate [16–20]. There are three main laser-based methods to produce coatings: laser chemical vapor deposition (LCVD); pulsed laser deposition (PLD), and laser cladding. In both LCVD and PLD there is no need of using powder or wire. In the third group, material in the form of blown powder, or a wire feed is typically added to a substrate via a thermally induced melt pool to achieve a surface layer with desirable dimensions and mechanical properties. The main role of the laser in these types of processes is to generate the concentrated heat source which creates a melt pool allowing the deposited material to fuse to the substrate. The influence of various process parameters such as feed rate, hatch spacing, powder size distribution, deposition pattern, input energy, etc. have all been widely studied [21,22]. While there is little doubt in the effectiveness of deposition using these techniques, due to the fact that these techniques are thermally driven, voids, phase changes, inconsistent diffusion, microcracks, anisotropic grain structures, and crystallographic texture are expected to occur [23,24]. Furthermore, issues related to the residual stresses in the cladded parts that lead to high hardness and distortion as well as anisotropic properties that develop in the laser-cladded components are other drawbacks of the laser cladding technique that need to be fully controlled in order to use this technique for the fabrication of functional components [25–29]. Additionally, due to the large temperature gradient between the low-temperature substrate and the high-temperature melt pool, rapid solidification of the molten material can lead to relatively weak bonds between the substrate and the newly deposited material if improper process parameters are used. This problem has been mitigated to some extent in techniques such as blown powder laser cladding, but it still remains a limitation in other laser-based cladding techniques. Although precise control over process parameters can mitigate detrimental microstructural variations and enhance the uniformity of the bonded material which leads to improved mechanical properties [30], there are still several impediments to the widespread utilization and adoption of laser-based deposition technologies [24,31]. Considering all these challenges, exploring a more efficient cladding process is of immense interest.

The aforementioned issues have led to the onset of solid-state laser-based joining processes which can be implemented for the coalescence of dissimilar materials in their solid-state without actually melting them. In solid-state welding, typically, the bonding is achieved through generating plastic deformation of the parent materials by implementing different forms of energies [1]. While usually joining is resulted from the application of the pressure alone, in some cases, a combination of heat and pressure is also applied. However, in the latter scenario, the temperature stays below the melting temperature of the materials that are welded and the generated heat is not sufficient to results in any melting at the macroscale while localized melting might occur. The use of pressure and shock waves for joining dissimilar materials in processes such as explosive welding and magnetic pulse welding has been explored and commercialized in recent years [32–35]. In explosive welding an energy source is implemented to propel a moving flyer plate into a stationary substrate at very high velocities, creating a solid-state bond at the metal interface where metallic bonds are generated between metallic surfaces without any macrolevel melting [36]. This is achieved at high pressures which induce severe plastic deformation that deforms asperities on the surfaces and breaks through the oxide layers to form a bond between the two surfaces in the bonding region. The grains near the bond interface are typically refined due to the work hardening induced during the process. However, since the process is performed locally at the interface, grains in nearby regions do not exhibit any grain structure alteration. A wide range of materials including carbon steels, copper, nickel, gold, titanium, etc. have been welded together using this technique [37,38].

Laser impact welding (LIW) benefits simultaneously from impact welding and laser-driven flyers to join thin films (up to around 200 μm in thickness) of dissimilar materials [39–41]. This method is most suitable for thin metal foil joining, which is widely needed in micro-electronics, medical devices, batteries, etc. A main advantage of this method is its independency on the electrical conductivity of the cladding material and the substrate [32]. Similar to explosive welding, in this technique a flyer plate is accelerated to an extremely high velocity, in the order of a few hundred meters per second, with a high strain rate of around 10^6 s^{-1}, using a laser pulse to create a bond with a substrate. Wang et al. [42] studied the interface in aluminum-titanium specimens and reported that due to the uneven vertical impact pressure present in LIW, several areas referred to as the smooth interface, intrusion structure, nanocrystal structure, diffusion structure, and the porous structure were formed. The uneven and wavy nature of the interface in LIW has also been reported previously in several different reports [43–45] and has been extensively discussed by Zhang et al. [32]. However, in contrast to other similar methods, the geometry of the waves varies throughout the length of the bond [42]. The lower and more localized energy input used in this technique, when compared with similar methods such as explosive welding, results in less disturbance to the microstructures in areas adjacent to the weld-spot [46], and the grain refinement only occurs up to a distance of about 10 μm from the boundary of the weld-spot [47]. Transmission electron microscopy revealed the diffusion of atoms between both the thin film and the substrate [42]. Additionally, “island diffusion” (i.e., non-continuous and localized diffusion) of the thin film material into the substrate was also observed and attributed to micro-level melting phenomenon. Therefore, it can be concluded that the intensity of this diffusion is affected by both the impact velocity and the melting temperatures of the metals being bonded together [48].

While the developed solid-state cladding processes are superior and more desirable compared to fusion-based techniques due to their outstanding attributes such as fabricating joined materials with less defects, lower tensile residual stresses, and more uniform mechanical properties, deficiencies such as the presence of porosities still appear as problems. This has led to the demand for more efficient solid-state joining processes that not only can be implemented for the fabrication of structures with a lower density of defects and residual stresses but also with more uniform distribution of microstructures and mechanical properties. Herein, a relatively new process, called high-velocity laser accelerated deposition (HVLAD) is reported. This technique was first introduced by Hackel et al. in Lawrence Livermore National Laboratory, USA [49,50], but further studies in academia were very limited. This method can be used to clad a thin film onto a substrate to create a thin protective coating using pressure waves generated from intense laser pulses. Since HVLAD is a solid-state process, it eliminates prevalent problems such as significant microstructure evolution, hot cracking, elemental segregation, and high level of destructive tensile residual

stresses that are attributed to the fusion-based techniques [51–55]. Also, since the process is conducted without melting or introducing a liquid phase, the presence of fine dispersoid particles or particles which have different densities and melting points than the base material has been eliminated. Furthermore, the process is applicable to thin metal foils without creating any warping or deformation. Modifications implemented in this technique, such as the removal of the spacers between the thin film and the substrate, distinguishes this method from LIW, and results in higher efficiency and more facile setup preparation. The role of the water overlay (confining media) and the ablative layer (vinyl tape) in this process are also carefully studied and the results indicate a significant increase in inducing pressure using the confined mode. The higher pressure applied during the cladding in the confined mode compresses the pores which lowers defect density per volume and eliminates the necessity of conducting time-consuming postprocesses. While in the unconfined mode, with the absence of the confining water

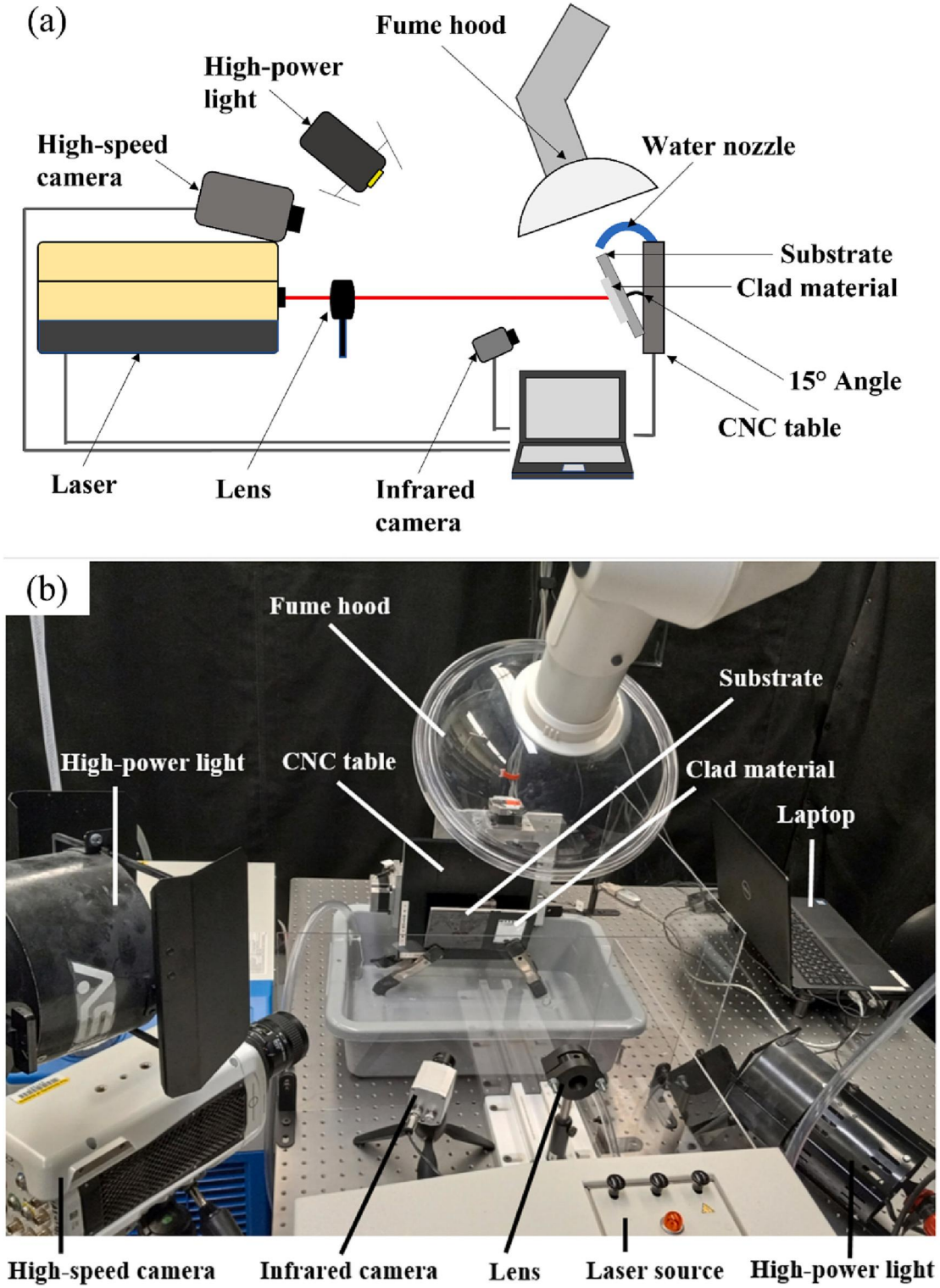

Fig. 1. (a) A schematic of the setup for the cladding process and (b) an image of the setup with different instruments labeled.

media and the ablative overlay, a transition in the deposition process was observed in which the mechanically-driven deposition process appeared to exhibit thermal effects which resulted in microlevel melting at the interface.

2. Experimental method

The experiment was conducted using a Q-Switched Nd:YAG laser (Powerlite DLS Plus), operating at a frequency of 10 Hz, a wavelength of 1064 nm, a power density of 6 GW/cm^2, and a pulse duration of 8 ns with a 3 mm diameter circular spot size at The University of Alabama. These specific process parameters were selected to ensure that the aluminum would properly adhere to the steel substrate. Preliminary tests proved that higher laser intensities tore the aluminum foil apart through a combination of thermal effects and high pressure, and the lower laser intensities were not sufficient for accelerating the thin film into the substrate. All tests were performed at room temperature in an open environment. The laser beam spatial shape had a high-order super-Gaussian profile. In this process the 1100 aluminum foil (10 μm thick) with dimensions of 3 × 3 cm was placed onto a ST14 steel substrate with a width and length of 10 cm and 10 cm, respectively. The aluminum foil was placed on the steel plate, and it was stuck and sealed with adhesive tape all around it in the shape of a square. By doing this, it was ensured that the foil was in contact with the steel plate and there was no clear gap between them. The target plate (steel) was large in all dimensions relative to the clad material (aluminum) and was angled 15° from perpendicular to the laser as shown in Fig. 1(a). The cladded area was approximately 10 mm × 10 mm, and three different cladding patterns were tested (simple matrix, simple hexagon, and face-centered) as shown in Fig. 2(a-c). The surface of the substrate was lightly polished using 4000 grit grinding paper before the cladding process to provide a clean surface for HVLAD. The cladding experiments were tested in two different modes: (1) without any confining media (unconfined mode, also known as direct ablation), and (2) with both water as the confining media and vinyl tape as the ablative layer on the thin film (confined mode). The primary purpose of using the vinyl tape as the ablative overlay in the confined mode is to enhance the formation of the plasma on the surface of the clad material. This ablative layer is also used to mitigate the thermal effects on the clad material, making it a primarily mechanically-driven process.

After the cladding process was completed, the specimens were cut using a Mitsubishi FA20S Wire-EDM machine using a standard 250 μm brass wire (Cu—36Zn) in a DI-water dielectric tank. Subsequently, the specimens were mounted and polished through standard metallurgical procedures. This included grinding the samples using a mechanical polisher with 240, 600, 800, 1200, and 2400 grit SiC grinding pads, followed by 3 and 1 μm colloidal silica suspension solutions. After mechanical polishing, mounted specimens were polished on a vibratory polisher with a 0.05 μm colloidal silica suspension solution for 24 h.

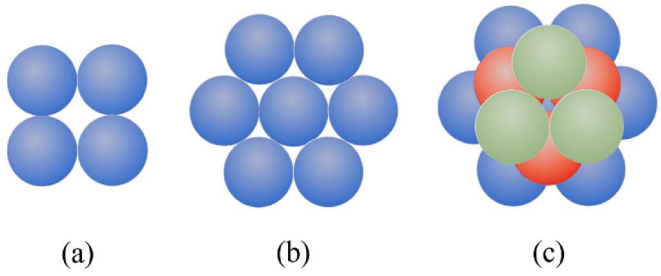

Fig. 2. Different deposition patterns including the (a) simple matrix, (b) the simple hexagon, and (c) the face-centered pattern. The face-centered pattern includes three layers. Each pattern was used to deposit a single layer of aluminum. Subsequent layers were only added after each pattern was completed.

Both the top and cross-sectional views of the cladded substrate were characterized using a scanning electron microscope (Apreo FE-SEM) equipped with electron back scatter diffractor (EBSD). An acceleration voltage of 30 keV was used at a working distance of approximately 16 mm from the SEM column with a step size of 0.1 μm.

The nanomechanical properties of the thin film (aluminum foil) before the cladding process, the substrate, and the cladded material after multiple layers of cladding using both cladding methods were all obtained using an instrumented nanoindenter (Anton-Paar, TTX-NHT^2) equipped with a diamond Berkovich tip. Nanoindentation tests were conducted with a 15 s dwell period at a maximum load of 25 mN. The surface morphologies were studied using a KEYENCE VHX-7000 optical microscope with a VHX-7100 optical head as well as a profilometer (KLA Tencor D-500). A compact professional thermal imaging camera (FLIR C2) was also used to measure the temperature distribution over the surface of the specimen during the cladding process, and a Vision Research Phantom V611 high-speed camera was used to record the event. The recording was saved into a series of images utilizing a framerate of 55,000 fps. A schematic of the setup and the actual setup used during the cladding process are provided in Fig. 1(a) and 1(b), respectively.

3. Results and discussion

During the confined method, the high peak power laser beam is propagated through a non-compressible transparent tamping layer, herein, a thin layer of running water. After passing through the water, the laser beam interacts with either an ablative layer or the actual material surface. The intense irradiance of the light (typically 0.2–10 GW/cm^2) ablates a thin, micrometer-range, layer of surface material creating and heating a plasma in <1 ns to a temperature in the range of 15,000 K. The plasma conforms itself to the contour of the clad material surface and generates a pressure pulse [56–60]. This accelerates the dense metal foil (referred to here as the clad material) over a very short duration of time, typically a few nanoseconds, in the range of hypersonic velocities. While the clad material is on top of the substrate, a small gap, approximately around 20–30 μm, exists between the two. The oblique substrate causes the impact process to generate intense shear stress. When the clad material collides with a high velocity and with a very high pressure that exceeds the yield stress of the cladding material, plastic deformation and bonding with the substrate are accomplished. While the nature of this bonding needs additional studies, it is hypothesized that the impact pressures are high enough to bring the surface atoms into direct contact, creating a high strength chemical or metallic bond. Also, severe plastic deformation at the interface can lead to mechanical alloying. The specimens fabricated using the confined method were typically much smoother than those fabricated using the unconfined method (Fig. 3(a-i)).

In the unconfined mode, the laser interacts with the surface of the clad material and the plasma is formed directly at its surface. In this case, the plasma dissipates as soon as the laser pulse ends in several nanoseconds, and much smaller pressure waves are generated. The lack of the ablative overlay intensifies the thermal effects of the laser at the surface of the clad material. Also, since there is no confining media to prevent the plasma from expanding away from the surface of the clad material, the induced peak pressure and the duration of the pressure wave are both reduced. The specimens fabricated using the unconfined method were much less uniform and exhibited more sporadic bonding as compared to those fabricated using the confined method (Fig. 3(a-i)). These optical images indicate the difference in the two cladding methods and highlight the transition from a primarily mechanically-driven process to one in which thermal effects are also present in the absence of the confining media and the ablative overlay.

One also needs to consider how the ablative layer influences the cladding process in the confined mode. The ablative layer is composed of a solid material on one side, and an adhesive on the back side. When an

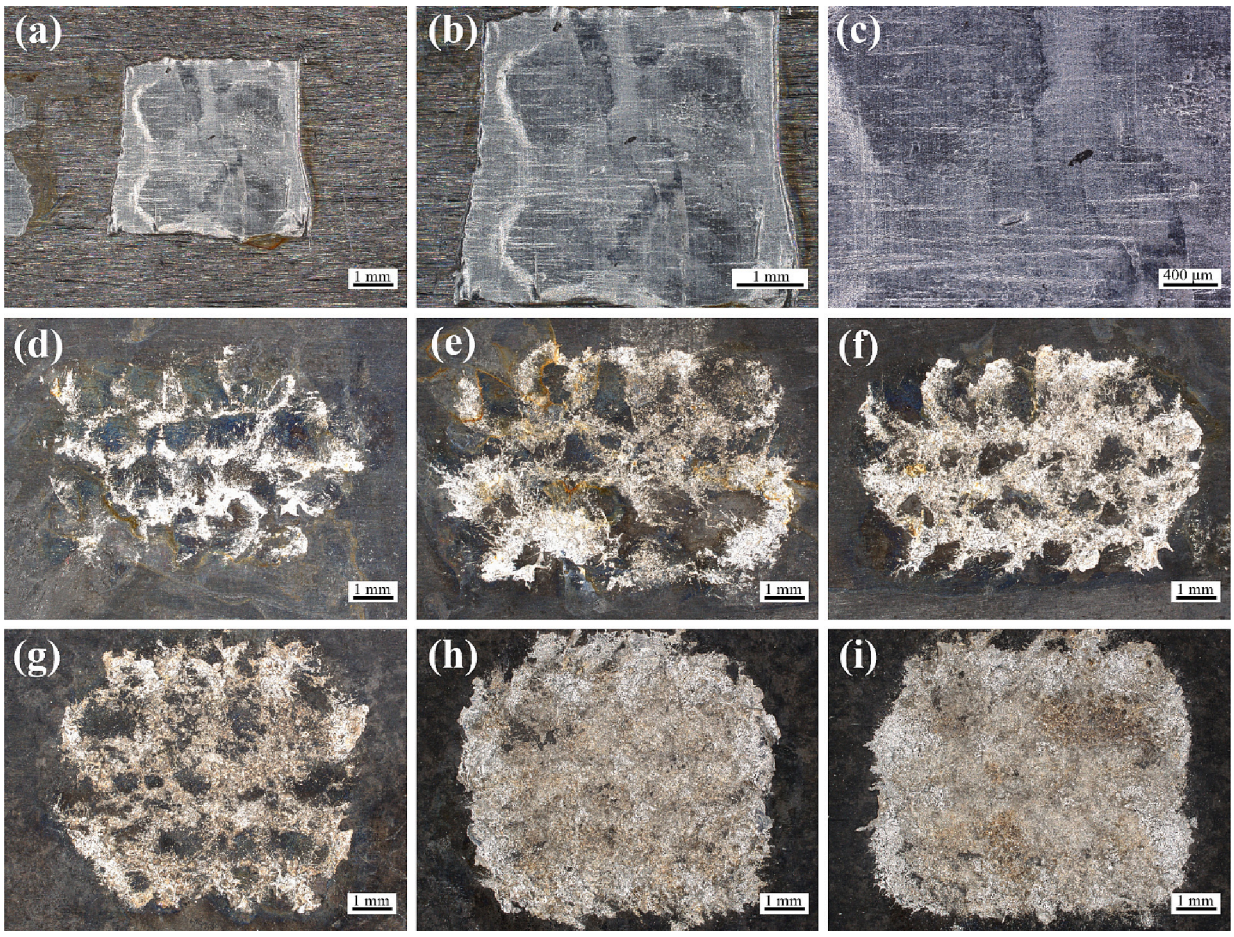

Fig. 3. Optical microscopy images of the specimens cladded using the confined mode (a-c) and the unconfined mode (d-i). (a) A single layer using the simple matrix surface coverage pattern; (b) and (c) are higher magnifications of (a); (d), (e), and (f) are 1st, 2nd, and 3rd layers of deposition using the simple hexagon surface coverage pattern depicted in Fig. 2(b), respectively; (g), (h), and (i) are 1st, 2nd, and 3rd layers of deposition using the face-centered surface coverage pattern depicted in Fig. 2(c), respectively.

ablative overlay such as vinyl tape is used, the sound travels faster in the denser solid side of the tape than the adhesive back side. Since the product of sound speed and density is greater in the solid side of the tape, the resulting pressure wave is reflected when the leading edge of the pressure pulse reaches the interface between the solid and adhesive interface of the tape, and a large portion of the initial pressure pulse is reflected back into the tape and back toward the plasma. The amount of pressure that is released into the adhesive is sufficient enough to not only compress the adhesive, but to also accelerate the aluminum foil into the steel substrate. The part of the pulse that is reflected back into the tape reaches the plasma and then fully reflects off of the dense plasma which directs it back into the tape. However, since the adhesive was compressed by the earlier part of the pulse, and since it has a very low reflection coefficient, the majority of the pressure is propagated into the film. The film has already begun to move due to the earlier acceleration, so the strong pressure pulse is now more effective than moving the film from a stationary position. This leads to better bonding between the aluminum foil and the steel substrate.

Similar to the LIW process, the properties of the clad material and its interface with the substrate are widely dependent on the process parameters which include the impact angle, impact velocity, mechanical properties of the materials, energy density, etc. [41]. The surface coverage index (SCI), which is the fraction of surface of the target material that is occupied by clad material after cladding, also depends on the number of layers and the cladding pattern. These process parameters need to be optimized to achieve the desired mechanical and morphological properties. For instance, excessive velocity can cause major melting that encourages intermetallic formation. This can also lead to brittleness or spalling in the impacting plates. Fig. 2(a-c) show the three different surface coverage strategies, namely, simple matrix, simple hexagon, and face-centered, that were tested here. Each surface coverage pattern displayed in Fig. 2(a-c) corresponds to one instance of each pattern, meaning that a new layer of the clad material (aluminum foil) was placed onto the steel substrate for successive layering only after each pattern was completed. Fig. 3(d-i) compare the morphology of the achieved clad layers using these patterns in both the confined and unconfined modes. In the unconfined mode, it can be observed that the clad layer obtained by the face-centered pattern has the highest SCI (almost 100 %), followed by the simple hexagon pattern, while the simple matrix pattern achieved the least SCI. By comparing Fig. 3(a-c) to (d-i), it can be observed that the confined method, which utilized the simple matrix surface coverage pattern depicted in Fig. 2(a), generated a more continuous structure than the unconfined mode which exhibited rougher, non-uniform bonding for the simple hexagon and face-centered surface coverage patterns, Fig. 2(b) and (c), respectively. This is due to the change in the deposition mechanism, where in the presence of the water and the ablative layer (vinyl tape), the high pressure generated by the plasma creates an impact force that leads to more effective bonding between the clad material and the substrate, while in the absence of the confining media and the ablative overlay, microlevel melting and solidification of the clad material were observed which led to nonuniform bonding and undesirable surface roughness.

The profilometry results presented in Fig. 4 compare the surface morphologies of the specimens cladded using both the confined (using

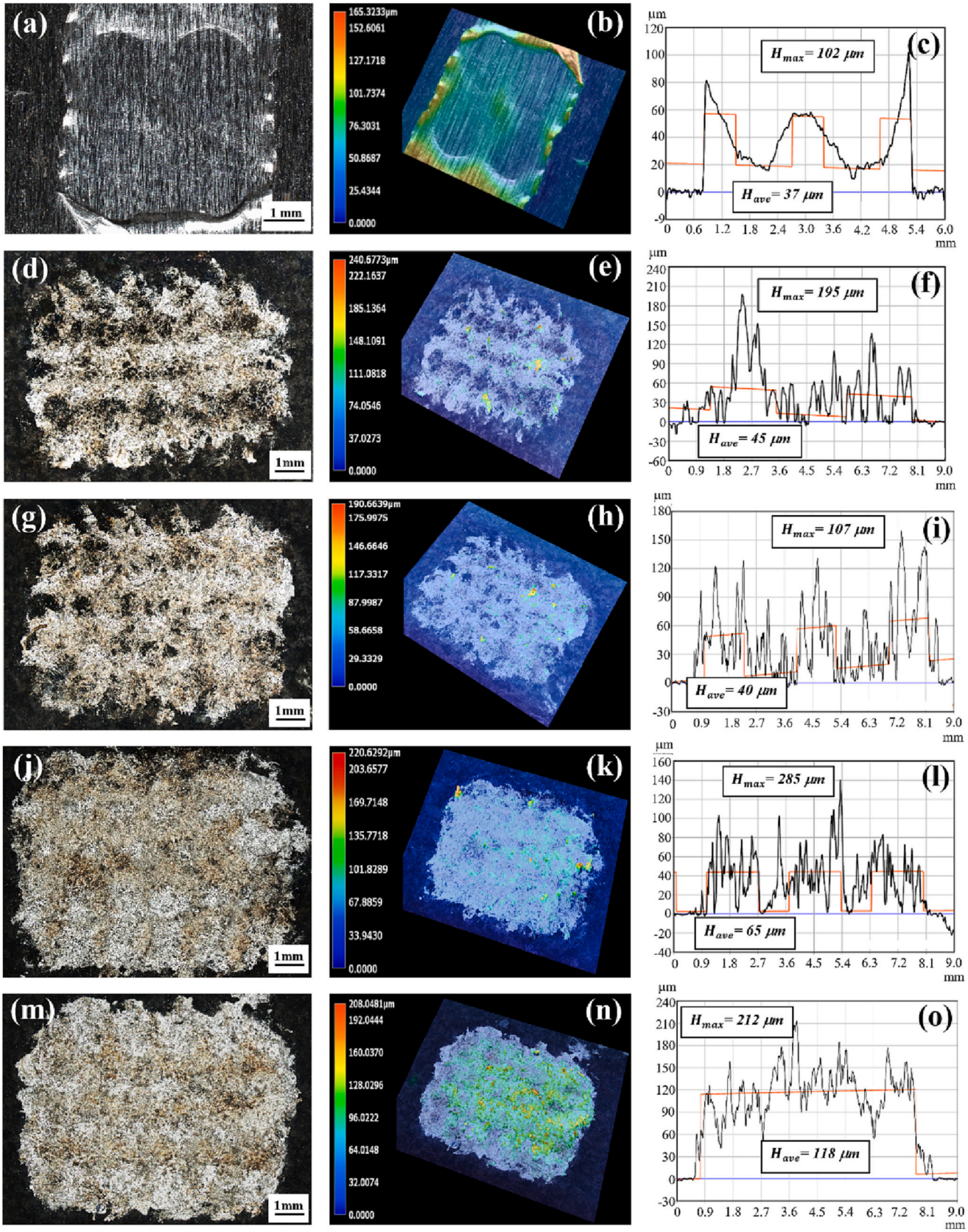

Fig. 4. Optical images, surface topography, and surface roughness profiles of: (a, b, c) A single layer using the simple matrix surface coverage pattern in the confined mode, and (d, e, f) one layer; (g, h, i) two layers; (j, k, l) three layers; and (m, n, o) four layers using the face-centered surface coverage pattern, depicted in Fig. 2(c), in the unconfined mode.

the simple matrix pattern) and unconfined method (using the face-centered pattern). It can be observed that when the confining media and the ablative layer were included, the average surface roughness was much smaller (Fig. 4(b) and 4(c)) even when cladding was performed with only a single layer using the simple matrix surface coverage pattern shown in Fig. 2(a). For the specimen cladded in the confined mode with the simple matrix surface coverage pattern, large peaks can be seen in Fig. 4(c) which correspond to the unbonded aluminum which peeled away at the edges. By observing Fig. 4(b) it can be clearly seen that uniform bonding is present where the laser contacted the surface of the substrate, while areas in between and surrounding the circular patterned shots appear to not be fully bonded to the substrate. This is due to the surface coverage pattern that was used (Fig. 2(a)) which did not include any overlap between successive shots. For the specimens cladded without any water or ablative layer (unconfined mode), as the number of layers increased using the face-centered surface coverage pattern, the average surface roughness decreased, and the surface exhibited reduced porosity. The addition of the confining media enhances the formation and prolongs the dissipation of the plasma. This leads to a greater concentration of the energy generated by the plasma and enhances the pressure wave generated by the plasma which accelerates the clad material into the substrate. It can also be seen that a single layer deposition using the simple matrix pattern in the confined method generated a relatively uniform clad layer with an average surface roughness of 37 μm (Fig. 4(c)). However, in order to obtain a uniformly cladded layer with a similar SCI using the unconfined method, four layers of the face-centered pattern were required (Fig. 4(m-o)).

Both tensile shear tests and peel tests have been employed in previous studies on laser impact welded specimens [61–63] to quantify the bond strength of the bonded material to the base material. While laser impact welding is inherently different than HVLAD, the two processes yield similar bond interfaces. In one study by Wang et al. [61] tensile shear tests were performed on laser impact welded weld joints. To do this the authors applied shear loads to both the welded aluminum and the brass base plate. The recorded loads for tensile failure were measured between 9.57 and 17.89 N with the maximum failure load ~62 % of the tensile failure force of the brass base plate. In another similar study by Wang et al. [62] peel tests were applied perpendicular to weld surfaces to evaluate the bond strength between laser impact welded aluminum on titanium. Results from the load transducer showed that the average peel force was between 1.61 and 3.41 N for nuggets with a diameter of 4 mm and 2 mm. The one with 4 mm spot size had larger peel force than the one with 2 mm spot size. The authors also observed that laser impact welding performed at a larger standoff distance (100 μm versus 75 μm) required a larger peel force. This was attributed to the higher velocities that were realized by the aluminum flyer plate at a greater standoff distance. It is important to note that the large variations in the measured failure forces in these two studies may not only be attributed to the materials, but also to the bond strength measurement techniques which were performed either perpendicular or parallel to the bond interface. In another study by Sadeh and Malik [63] tensile shear tests were also used to evaluate the bond strength of aluminum which had been laser impact welded, followed by laser peening to brass, copper, and stainless steel plates. Forces were applied parallel to the bond interface as done by [62]. Results indicated that when the weld was stronger than the aluminum foil, tearing occurred in the aluminum. This was noted as the predominant failure mechanism across all the specimens. The average maximum load to failure exhibited by the LIW specimens which had aluminum bonded to stainless steel was measured to be 13.89 ± 1.36 N for a nugget with a diameter of ~3.00 mm. This value increased slightly with one laser peening shot but decreased to within standard deviation of the average maximum load exhibited by the LIW specimen after two laser peening shots. While these results highlight deviations between the two bond strength characterization methods, they also provide some insight into the bond strength that might be exhibited by the cladded specimens here. From these results it can be hypothesized that using tensile shear tests the bond strength of the cladded aluminum on the ST14 steel cladded in the confined mode (Fig. 4(a)) will be on the order of 10–18 N. Investigation into the bond strength of the specimens cladded in the confined mode will be explored in future work. The interface between the clad material and the substrate after cladding was studied using a scanning electron microscope (Fig. 5(a-b)). The interface is relatively flat in both methods, but a slight wave-like pattern can be observed in specimens cladded in the unconfined mode. This pattern has been reported in other similar processes where the bonding is created using a high velocity impact [32,35,64]. The wave-like morphology at the interface not only increases the surface area at the contact line, but also enhances the bonding between the two metal interfaces and creates a “mechanical interlocking” mechanism. However, it has been reported that in explosively welded metal combinations [65–67], a flat interface is not indicative of weak bonding and a wavy interface is not always necessary for strong bonding. The less wavy nature of the interface in the current report, might be attributed to the absence of a large space (i.e., in the order of a few hundred microns) between the thin film and the substrate [67] and only having around 20–30 μm of space that leads to a lower impact velocity compared to LIW. Small microstructural defects such as porous inner architectures, voids, and microcracks were observed in the cladded material using both cladding techniques (Fig. 5(a-b)), but a much higher defect density was observed in specimens cladded using the unconfined method (Fig. 5(b)). These defects are similar to what was reported before in other high velocity joining techniques [68–72]. Additionally, for the specimens that were cladded in the unconfined mode, as the number of layers increased, the defect density decreased, which was likely attributed to the “compaction” of the layers due to the increasing SCI. The formation of these porosities indicates that in addition to the primary mechanical forces which drive the process, in both the confined and unconfined modes, microlevel melting and solidification also take place at the interface during the deposition process. A higher density of defects in the specimens cladded in the unconfined

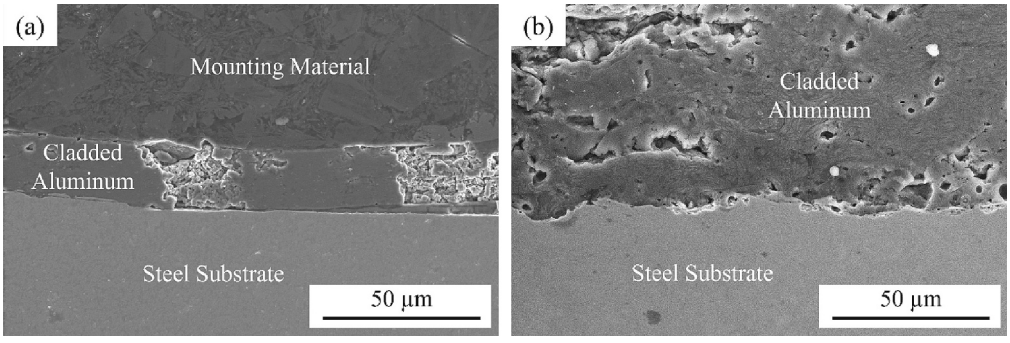

Fig. 5. SEM images of the interface in a specimens cladded (a) in the confined mode with a single layer using the simple matrix surface coverage pattern depicted in Fig. 2(a), and (b) in the unconfined mode for four layers using the face-centered surface coverage pattern depicted in Fig. 2(c).

method can be attributed to a higher level of microlevel melting which provides a favorable condition for the porous structure formation in all of the specimens. There were also no obvious interfacial lines between the cladded layers when several layers were applied using the unconfined technique (Fig. 5(b)). The scanning electron microscopy images indicate that the layers form a uniform coating of material without any discontinuities at the interface of successive layers.

While high-velocity impact welding is commonly known as a solid-state manufacturing process, the formation of microstructural defects within the bonding area as a result of melting phenomena indicates that this process does not occur entirely in the solid-state zone [73]. Similarly, as indicated above, the HVLAD process is accompanied with some defects in regions close to the interface that are attributed to the local temperature increase at the bonding interface (Fig. 5(a) and 5(b)). Since this is a high-speed phenomenon, studying the rapid change in the pressure and temperature cannot be performed readily and requires advanced tools. In order to investigate the thermal effects and evaluate the correlation between microlevel melting and the formation of porous structures and other microstructural defects, a high-speed camera was used to take sequential images of the process (Fig. 6(a) and 6(b)). The presence of what appear to be molten droplets, which can be seen when performing cladding using the unconfined method in Fig. 6(a), is presumed to be attributed to the solid-to-liquid transition during cladding which encourages the formation of porosities in the cladded material. This can be explained by the model that Rice et al. [74] developed, describing that sudden temperature rise and subsequent rapid cooling under isochoric conditions where the volume of the closed system undergoing a process remains constant encourages the formation and growth of voids. By comparing the brightness of the droplets presented in Fig. 6(a) and 6(b) it can be observed that the droplets in Fig. 6(a) are significantly brighter than those in Fig. 6(b). Since metal has a higher reflective index than water, and since water not only reflects light but also refracts it, it is understood that water will have a lower brightness than steel when imaged on the same device with the same brightness and frame rate. As such, it appears that water droplets are present in Fig. 6(b) rather than molten metal droplets, and if there are small metal droplets present during confined cladding, they are difficult to detect due to the water overlay which acts as a "blanket".

Nasiri et al. [73] indicated that the LIW process is not isochoric (a constant-volume process), and the formation and coalescence of the voids are attributed to expansion of the flyer plate (herein, the cladding material) as a result of rapid heating/pressurization followed by contraction due to the cooling/depressurization. It is hypothesized that this is the main reason for the formation of the porosities in the specimens. However, both of these hypotheses require further investigation which will be covered in future work. The rapid heating-cooling steps are accompanied by the circular motion of the molten materials and the extreme thermal gradient at the interface which encourages the formation of the microcracks in this zone. The traces of circular motion of the molten material can be seen in the pattern observed in the SEM images of the solidified cladded material in Fig. 7(b). This circular motion assists with the "mechanical interlocking" as well. The trace of circular motion is not seen in Fig. 7(a), which lends credence to the hypothesis that microlevel melting is not as prominent when cladding using the confined method as opposed to the unconfined method.

Given that this process occurs in an extremely short period of time (typically, a few μs), and that the temperature gradient is very localized, there is not sufficient time for heat to transfer away from the interface. Thus, microlevel melting and temperature variations are primarily limited to the interfacial region. A FLIR thermal camera was used to evaluate the temperature increase in the vicinity of the cladded region just as the laser contacted the surface and just after the laser contacted the surface. Fig. 8(b-c) and 8(d-e) show the sequential images of the process for both the unconfined mode and the confined mode, respectively. It can be observed that the temperature increase is very localized, rapidly dissipates, and is almost negligible at the macrolevel over the surrounding material using both cladding methods.

Microstructual analysis of the interface was conducted using EBSD. The EBSD data of the substrate for both the unconfined and confined modes (Fig. 9(a) and 9(b), respectively) show evidence of grain refinement which is likely a result of high-pressure impact, and subsequent plastic deformation inherent to the HVLAD process. The grain refinement is proposed to be a result of dynamic recrystallization, where new grains nucleate and grow within regions of severe plastic deformation, normally when temperatures are above 0.5 $T_{melting}$. Of course, in this instance, the substrate is subjected to minimal heating, but it was shown in [75] that the temperature component of the dynamic recrystallization threshold reduces with increasing strain rates. The strain rates experienced by the substrate surface are similar to those which occur during laser peening $\sim 10^6\ s^{-1}$ which lends credence to the hypothesis that dynamic recrystallization occurred. Grain misorientation angle plots taken from the substrate surfaces (marked by white dotted lines in Fig. 9(a) and 9(b)) are presented in Fig. 9(c) and 9(d) for the specimens cladded using the unconfined mode with the face-centered pattern for four layers and the confined mode with a single layer using the simple matrix pattern, respectively. For the specimen cladded with one layer using the simple matrix pattern (confined mode), a large number of low-angle (2–15°) grain boundaries are present in addition to the high angle (> 15°) grain boundaries which existed within the steel substrate prior to cladding (Fig. 9(d)). The low-angle grain boundaries are indicative of subgrains which formed as a result of the intense straining of the substrate surface during cladding. For the specimen cladded using the face-centered pattern for four layers (unconfined mode) the fraction of low-angle grain boundaries increased due to the increased strain which resulted from multiple laser impacts (layers) which further enhanced the process of subgrain formation as well as subsequent recrystallization (Fig. 9(c)). It can be surmised that dislocations were funneled into the low-angle grain boundaries and caused their misorientation angle to grow into large angle grain boundaries, otherwise known as recrystallization [76,77]. Some reports of similar processes have attributed grain refinement in this region to melting and solidification [73,78], however, this seems less likely since the grains are not oriented epitaxially [79]. Recrystallization has been reported in similar processes like impact welding, where a recrystallized layer a couple hundred nanometers thick was observed and attributed to the short localized heating and severe plastic deformation inherent in the impact process [80,81].

The difference in hardness between the thin film aluminum and the steel substrate made it difficult to maintain a smooth surface finish on the aluminum cladded layer. Thus, the EBSD results were obtained primarily from the steel substrate side of the cladding interface. Near the surface, significant grain refinement is present in the inverse pole figure (IPF) maps as shown in Fig. 9(a-b) up to 7.5 μm away from the interface, indicated by the dashed white line. Near the cladding interface, the average grain diameter by area fraction is 1.3 μm and 0.8 μm for the sample cladded in the confined mode with a single layer using the simple matrix pattern and the sample cladded in the unconfined mode with four layers using the face-centered pattern, respectively. The average grain diameter of these grains are significantly smaller than the grain size in the base material which has an average diameter of 5 μm. There is an increasing level of plastic deformation as one approaches the cladding interface which can be observed by the kernal average misorientation (KAM) maps shown in Fig. 9(e) and 9(f). In the KAM maps, the blue color indicates a low amount of deformation, while the green color represents a high level of misorientation between points, and thus relatively higher deformation to the crystal structure. The KAM map of this area illustrates the extreme plastic deformation caused by the strong shear motion between the clad material and the substrate upon impact.

The force-displacement curves from the indentation characterization have been shown in Fig. 10(a). The average nanohardness value for the thin aluminum foil before deposition was measured to be 48 HV. After cladding, this increased to 61.8 HV for the specimen cladded with a single layer using the simple matrix surface coverage pattern in the

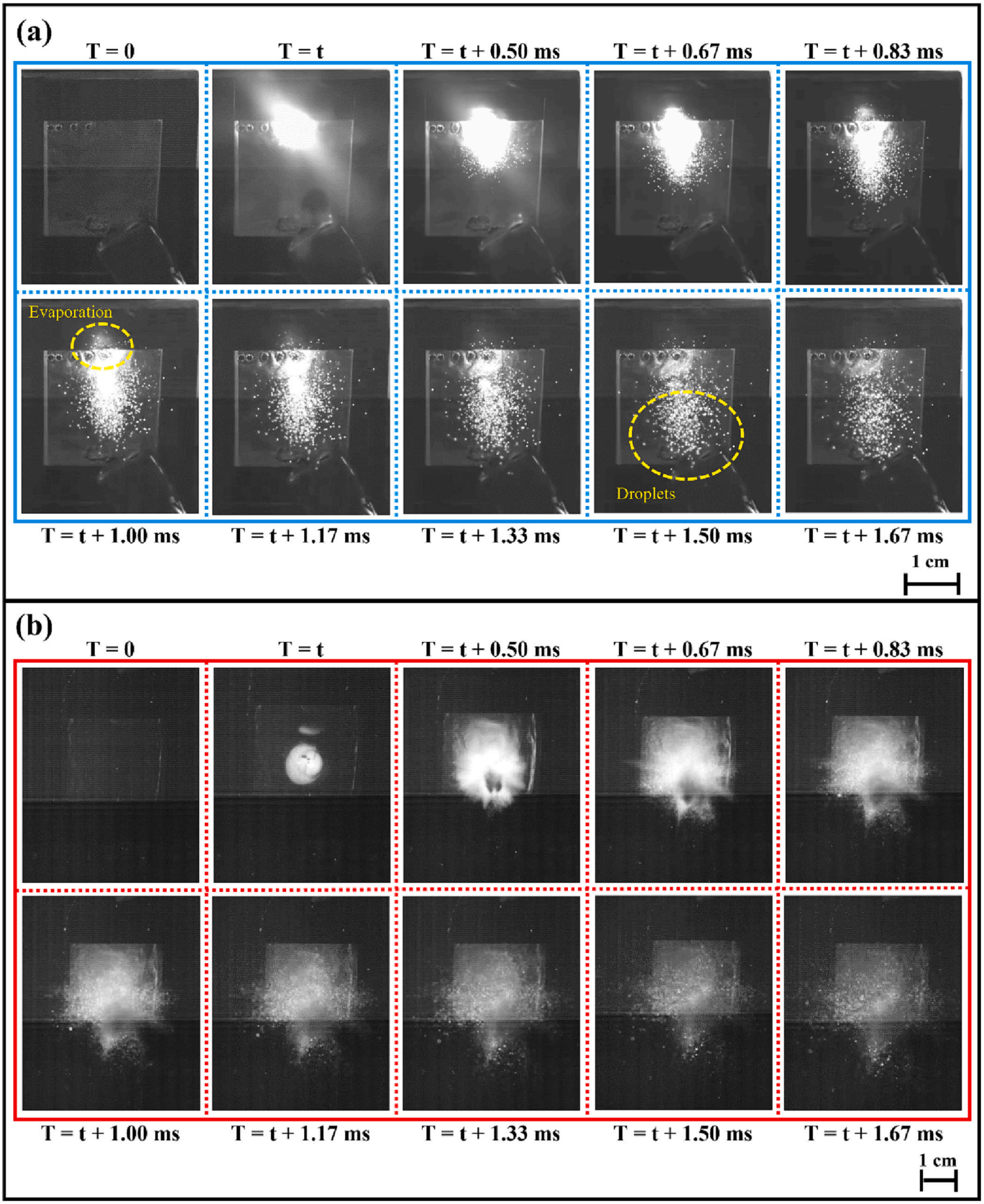

Fig. 6. Sequential images taken of the cladding process using a high-speed camera in the (a) unconfined mode, and the (b) confined mode. Videos S1 and S2 are available in the Supplementary Information section.

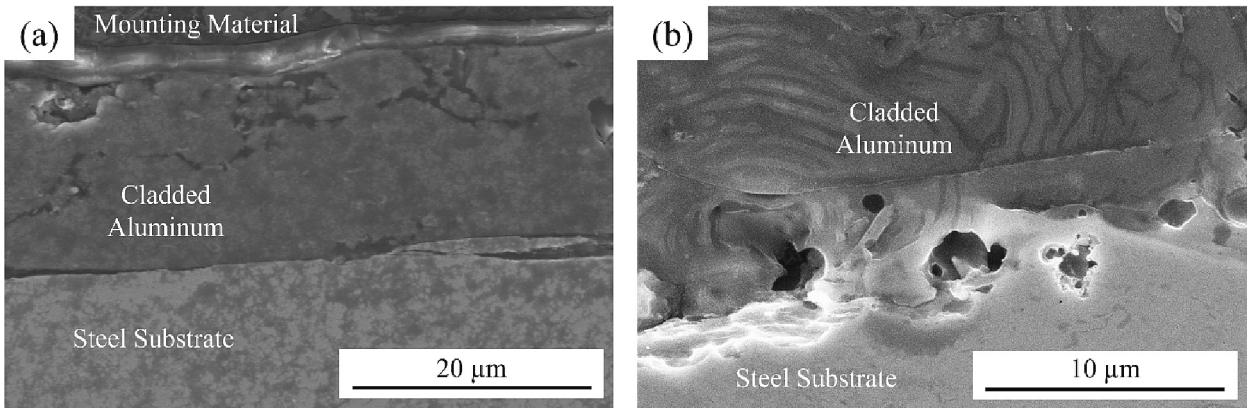

Fig. 7. The interface between the cladded aluminum and the steel substrate in specimens cladded in (a) the confined mode with a single layer using the simple matrix surface coverage pattern and in (b) the unconfined mode using the face-centered surface coverage pattern for four layers.

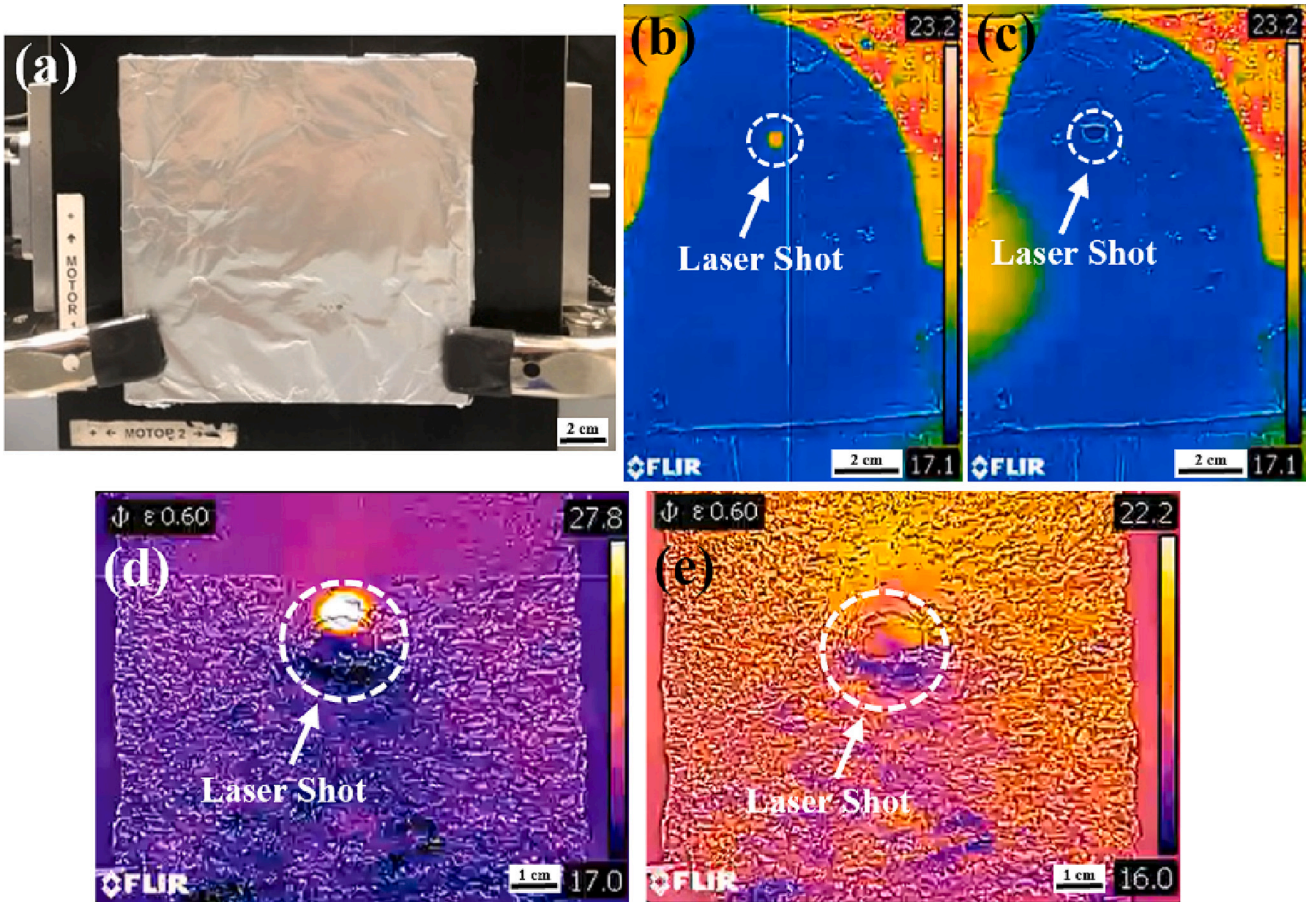

Fig. 8. (a) The setup for the cladding process with a thin layer of aluminum foil on a steel substrate, (b) an infrared thermal image of the substrate as the laser contacts the surface, (c) and after the laser pulse (~0.5 s after) in the unconfined mode, and (d, e) images of the cladding process in the confined mode corresponding to (b, c).

confined mode, 128 HV for a specimen cladded with two layers, and 156 HV for a specimen cladded with four layers using the face-centered surface coverage pattern in the unconfined method. The higher hardness is attributed to coldworking which resulted from the plastic deformation due to the high strain rate deformation process. Nanohardness measurements were also conducted across the cross section. For each sample 5 rows of indent were performed. As expected, a continuous increase in hardness was noticed across the interface from the cladded aluminum to the steel substrate (Fig. 10(b)).

4. Analytical modeling

While the work discussed thus far shows the mechanisms of laser cladding from an experimental perspective, it is useful to understand the underlying mechanisms which differentiate the confined and unconfined laser cladding methods. During laser cladding and similar processes such as laser peening, a pressure wave, is generated by the laser which propagates into the target material. In laser peening this mechanism generates a compressive residual stress field at the surface of the

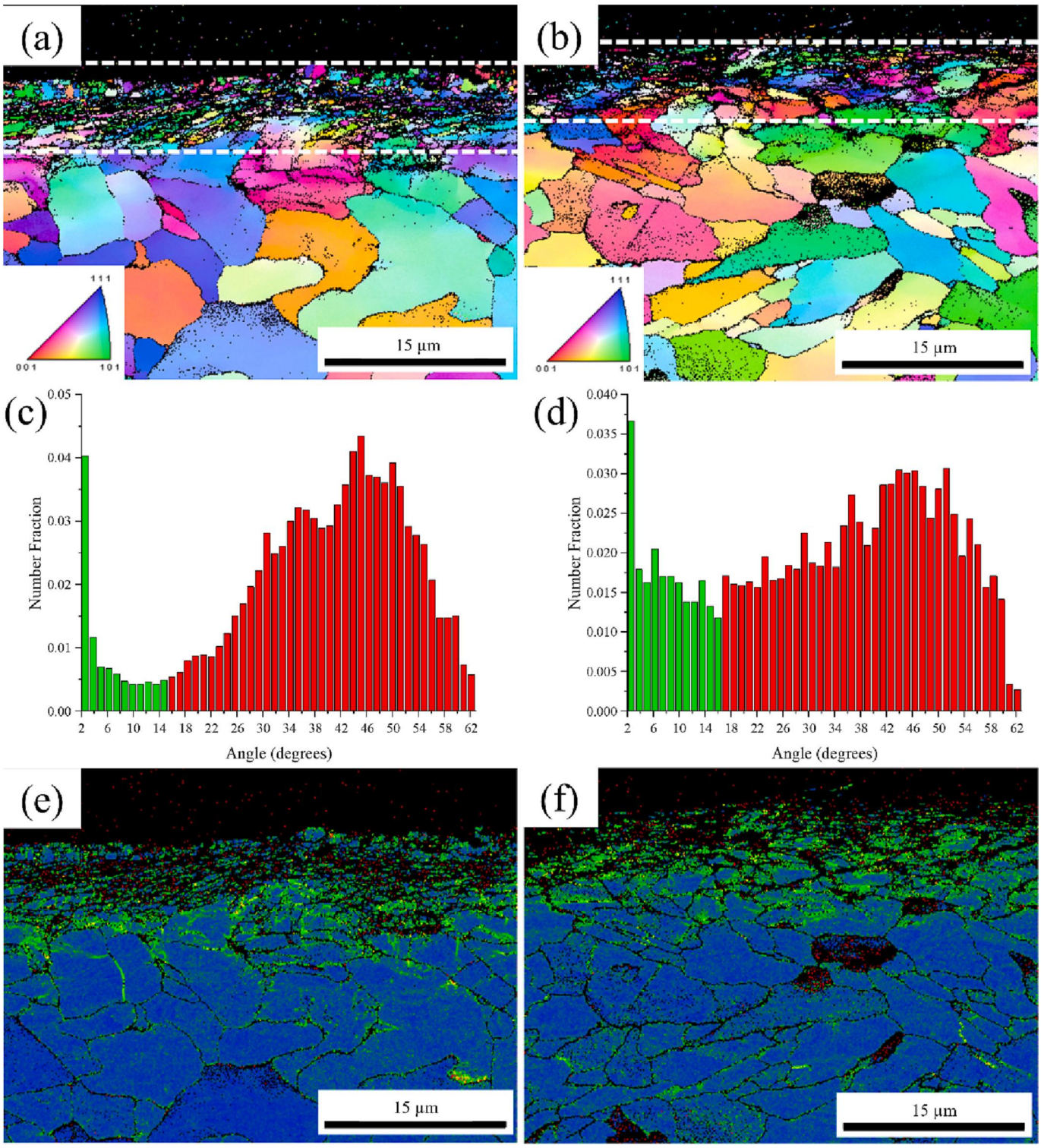

Fig. 9. Microstructure of the sample cladded in the unconfined mode using the face-centered surface coverage pattern for four layers (left column (a, c, e)) and of the sample cladded in the confined mode for a single layer using the simple matrix surface coverage pattern (right column (b, d, f)): (a, b) show inverse pole figure (IPF) maps of the cladded interface with the dashed lines showing the depth of grain refinement from the interface, (c, d) depict the grain size distribution for samples with the green bars indicating low angle grain boundaries (2–15°) and the red bars representing large angle grain boundaries (> 15°), and (e, f) Kernal average misorientation (KAM) maps (KAM maps show points with confidence indexes below 10 % as black pixels). (For interpretation of the references to color in this figure legend, the reader is referred to the web version of this article.)

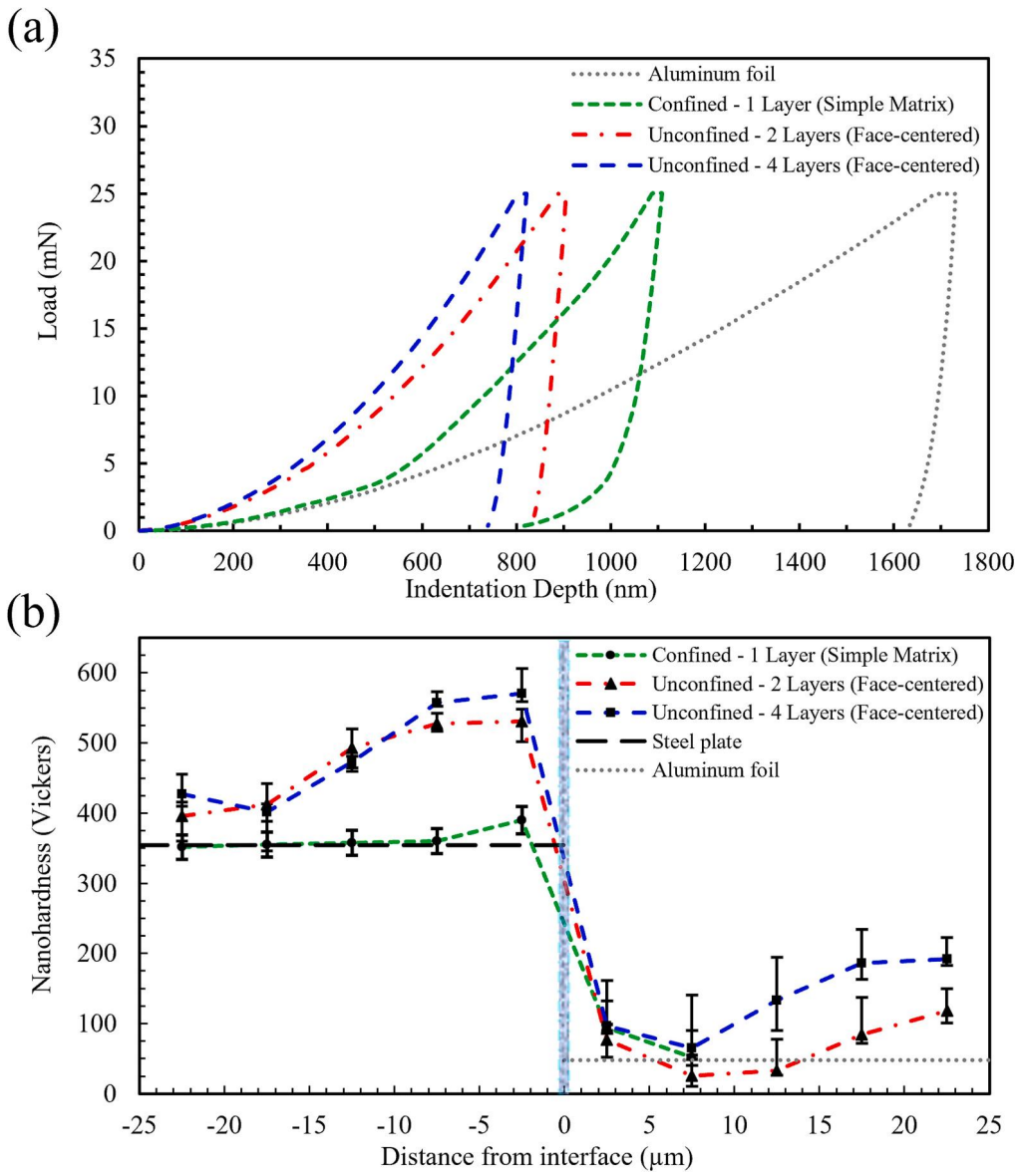

Fig. 10. (a) Force-displacement curves obtained from nanoindentation of the specimens cladded using both the confined and unconfined methods and (b) nanohardness measurements obtained from across the interface.

material. However, in laser cladding, the pressure wave is used to accelerate the clad material (1100 Al foil) into the substrate (ST14 Steel) as depicted in Fig. 11(a) and 11(b).

The water overlay and the vinyl tape are the confining medium and ablative layer, respectively. Fabbro et al. [82] have provided a set of equations that can be used to relate the plasma thickness $L(t)$ at time t (once the laser has contacted the material) to the laser intensity I_0 and pressure $P(t)$ of the wave generated by the plasma:

$$\frac{dL(t)}{dt} = \sum \frac{1}{Z_i} P(t) \tag{1}$$

where Z_i is the shock impedance of the materials in contact with the plasma. The laser intensity $I(t)$, which is the amount of laser energy absorbed per unit area, can be expressed by the following conservation of energy relationship developed from the Rankine-Hugonoit relations [83]:

$$I(t) = P(t)\frac{dL(t)}{dt} + \frac{d[E_i(t)L(t)]}{dt} \tag{2}$$

where $E_i(t)$ is the internal energy of the plasma. The thickness of the plasma interface is of particular interest when deriving a relationship between the plasma interface and the acceleration of the pressure wave. The relative acceleration of the pressure wave, which is a function of the area density m_i of the target material and any confining mediums which are the products of density ρ and thickness e of the materials (Fig. 11), can be expressed as:

$$\frac{d^2L(t)}{dt^2} = P(t)\left(\sum \frac{1}{m_i}\right) = P(t)\left(\sum \frac{1}{\rho_i e_i}\right) \tag{3}$$

Through the integration of Eqs. (1) and (3), Fabbro et al. [82] have defined the pressure $P(t)$ and velocity of the pressure wave at the end of the pulse duration t as:

$$P(t) = \left(\frac{m_i I_0 \alpha}{2t(\alpha+1)}\right)^{1/2} \tag{4}$$

$$V(t) = \frac{2P(t) \bullet t}{m_i} \tag{5}$$

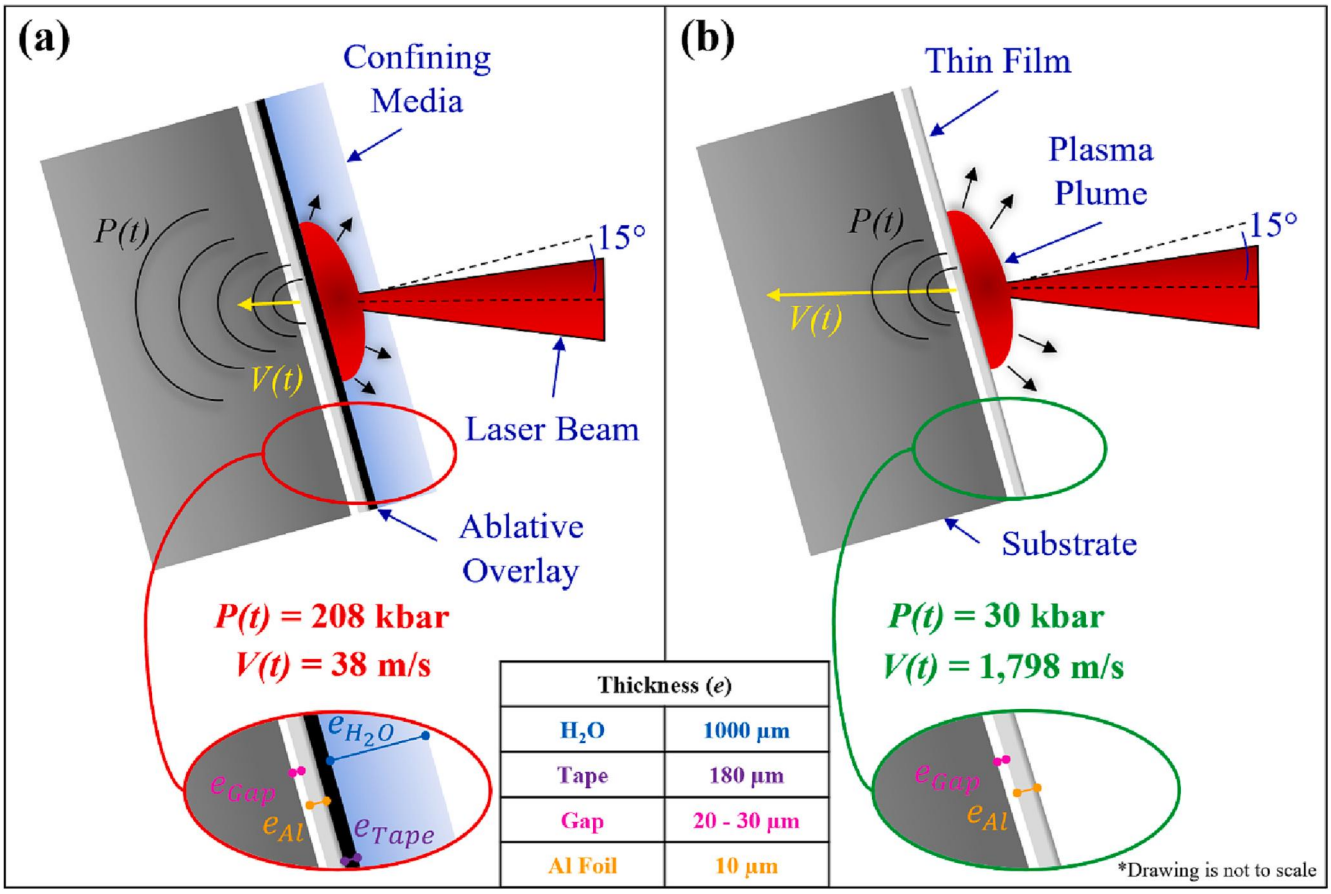

Fig. 11. Illustration of HVLAD process performed in both (a) confined and (b) unconfined modes.

The laser intensity, or power density, I_0 of the laser with units GW/cm^2 is obtained by dividing the laser energy (J) by the pulse width (ns) and the area of impact (cm^2). While α is the portion of the plasma thermal energy (typically 0.1 [82]).

Two cases were tested in this experiment: (1) without any confining media (unconfined mode – depicted in Fig. 11(b)), and (2) with both tape as the ablative material and water as confining medium (confined mode – depicted in Fig. 11(a)). For case 1, in the unconfined condition, only the area density of the 1100 Al foil was considered. The variables $I_0 = 6$ GW/cm^2, $\alpha = 0.1$, $m_{Al} = 2700$ kg/cm^2, and $t = 8$ ns were used to calculate the pressure and velocity of the pressure wave from the plasma which corresponded to 30 kbar and 1798 m/s, respectively.

For case 2, which includes the water overlay and ablative overlay (vinyl tape), an area density term for water m_{H_2O} and the vinyl tape m_{Tape} must be included. Consequently, Eqs. (4) and (5) are modified to:

$$P(t) = \left(\frac{\left(m_{H_2O} + m_{Tape} + m_{Al}\right) I_0 \alpha}{2t(\alpha + 1)}\right)^{1/2} \tag{6}$$

$$V(t) = \frac{2P(t) \bullet t}{\left(m_{H_2O} + m_{Tape} + m_{Al}\right)} \tag{7}$$

where the area density of the 1 mm thick water overlay and the 0.18 mm thick vinyl tape are 997 kg/cm^2 and 1380 kg/cm^2, respectively. Here it can be seen that the inclusion of the confining media and ablative layer (water and vinyl tape, respectively) increases the wave pressure to 208 kbar while decreasing the pressure wave velocity to 38 m/s.

The analytical model gives insight into the reasoning behind the varying results seen conducting HVLAD in both confined and unconfined modes. The purpose of a confining media is to concentrate the plasma expansion such that the duration of the pressure pulse is extended beyond the duration of the laser pulse which increases the impulse momentum transferred to the cladding material and likely changes the bonding characteristics under the experimental conditions tested in this work.

5. Conclusion

Herein an advanced cladding technique for joining dissimilar metals based on a direct extension of laser peening as a solid-state deposition method, namely HVLAD, was reported. This work aims to provide a foundation for future development of this technology. Due to the flexibility that this process provides, it is assumed that by scaling-up this method and additional studies, HVLAD will be able to be implemented to deposit a variety of coatings precisely to complex surfaces in a highly controlled manner. The process involves a high-speed oblique collision (15° from perpendicular to laser) between the clad material and the substrate using the pressure pulse generated by a high-intensity nanosecond pulsed laser beam. In-situ thermal and high-speed imaging tools were employed during the HVLAD process to investigate temperature variations and to provide a closer look into the driving forces involved during HVLAD in both the confined and unconfined modes. Surface topography and profilometry measurements provided insight into the surface roughness and uniformity of the bonded material orthogonal to the deposition direction. Advanced characterization techniques like SEM and EBSD were implemented to investigate the interface between the substrate and the cladded material. SEM was implemented to assess the formation of nano/microscale porous structures, voids, and microcracks at the interface, and EBSD was used to investigate the grain refinement and misorientation between grains induced by severe plastic deformation. Nanomechanical measurements were also performed to assess the nanohardness across the interface of the specimens cladded

using both techniques. The following conclusions were drawn from the study described above:

- Grain refinement at the interface was observed in specimens cladded using both cladding methods (confined and unconfined). KAM maps indicated severe plastic deformation in the substrate in regions near the interface. The specimen cladded in the confined mode presented a larger fraction of low-angle grain boundaries near the interface.
- Nanomechanical characterization tools were employed to evaluate the change in the hardness of the cladded layers and its dependency on the number of the layers as well as the change in the hardness across the interface. A significant increase in hardness was observed as the number of layers increased for the specimens cladded in the unconfined method.
- An analytical method was implemented to estimate the effects of introducing a confining water media and an ablative overlay on the pressure and velocity of the pressure wave which propelled the thin film during the confined process. Using this analytical technique, for the confined mode cladding, an 8-fold increase in the pressure of the plasma generated pressure wave was calculated.
- No significant temperature variations were observed at the macro-level during HVLAD using either the confined or unconfined methods. Microlevel thermal effects were more prevalent in the unconfined cladding mode. The confined cladding method primarily took advantage of the mechanical effects associated with LP.

Supplementary data to this article can be found online at https://doi.org/10.1016/j.surfcoat.2023.129638.

CRediT authorship contribution statement

Author Contributions: Supervision, defining the project and experiments, writing, & funding acquisition, K.D.; Conducting Experiments, M.V., T.S., T.U., N.B., R.R., N.H.; Formal Analysis, K.D., M.V., L.H., N.B.; Review and Editing, K.D., N.B., M.V., L.H., N.H. All authors have read and agreed to the published version of the manuscript.

Declaration of competing interest

The authors declare that they have no competing financial interests or personal relationships that could have influenced the work provided here.

Data availability

Data will be made available on request.

Acknowledgment

The project was supported by the National Science Foundation, CMMI, Advanced Manufacturing Program (Award Number: 2029059).

References

[1] W. Li, V. Patel, Solid state welding for fabricating metallic parts and structures, Encyclopedia of Materials: Metals and Alloys 246-259 (2022), https://doi.org/10.1016/b978-0-12-819726-4.00012-0.
[2] M. Vural, Welding processes and technologies, Comprehensive Materials Processing 3-48 (2014), https://doi.org/10.1016/b978-0-08-096532-1.00603-8.
[3] Y. Qin, Z. Jiao, Z. Feng, N. Shi, J. Han, X. Wei, Influence of welding sequence on welding deformation of T-joint, Transactions on Intelligent Welding Manufacturing (2020) 83–97, https://doi.org/10.1007/978-981-15-6922-7_6.
[4] B.K. Panda, S. Sarkar, A.K. Nath, 2D thermal model of laser cladding process of Inconel 718, Materials Today: Proceedings 41 (2021) 286–291, https://doi.org/10.1016/j.matpr.2020.09.214.
[5] K. Li, L. Yang, Y. Deng, J. Lu, J. Hu, A novel two-step method for laser cladding process of aluminum alloy based on low-power pre-sintering, SSRN Electron. J. (2023), https://doi.org/10.2139/ssrn.4362494.
[6] M.K. Alam, A. Edrisy, J. Urbanic, J. Pineault, Microhardness and stress analysis of laser-cladded Aisi 420 martensitic stainless steel, J. Mater. Eng. Perform. 26 (3) (2017) 1076–1084, https://doi.org/10.1007/s11665-017-2541-x.
[7] J. Heigel, P. Michaleris, T. Palmer, In situ monitoring and characterization of distortion during laser cladding of Inconel® 625, J. Mater. Process. Technol. 220 (2015) 135–145, https://doi.org/10.1016/j.jmatprotec.2014.12.029.
[8] Z. Yan, W. Liu, Z. Tang, X. Liu, N. Zhang, Z. Wang, H. Zhang, Effect of thermal characteristics on distortion in laser cladding of Aisi 316L, J. Manuf. Process. 44 (2019) 309–318, https://doi.org/10.1016/j.jmapro.2019.06.011.
[9] R. Kumar, H. Dey, A. Pradhan, S. Albert, J. Thakre, M. Mahapatra, C. Pandey, Numerical and experimental investigation on distribution of residual stress and the influence of heat treatment in multi-pass dissimilar welded rotor joint of alloy 617/10CR steel, Int. J. Press. Vessel. Pip. 199 (2022), 104715, https://doi.org/10.1016/j.ijpvp.2022.104715.
[10] W. Jiang, Y. Luo, Q. Zeng, J. Wang, S. Tu, Residual stresses evolution during strip clad welding, post welding heat treatment and repair welding for a large pressure vessel, Int. J. Press. Vessel. Pip. 189 (2021), 104259, https://doi.org/10.1016/j.ijpvp.2020.104259.
[11] R. Grinon-Echaniz, P. Refait, M. Jeannin, R. Sabot, S. Paul, R. Thornton, Study of cathodic reactions in defects of thermal spray aluminium coatings on steel in artificial seawater, Corros. Sci. 187 (2021), 109514, https://doi.org/10.1016/J.CORSCI.2021.109514.
[12] M. Vaseghi, H. Zand, M. Sameezadeh, Mechanical bonding in cold roll-cladding of tri-layered brass/steel/brass composite, Int. J. Mater. Res. 111 (2020) 826–832, https://doi.org/10.3139/146.111951.
[13] P. Zamani, Z. Valefi, K. Jafarzadeh, Comprehensive study on corrosion protection properties of Al2O3, Cr2O3 and Al2O3–Cr2O3 ceramic coatings deposited by plasma spraying on carbon steel, Ceram. Int. 48 (2022) 1574–1588, https://doi.org/10.1016/J.CERAMINT.2021.09.237.
[14] V. Hutsaylyuk, M. Student, K. Zadorozhna, O. Student, H. Veselivska, V. Gvosdetskii, P. Maruschak, H. Pokhmurska, Improvement of wear resistance of aluminum alloy by HVOF method, Journal of Materials Research and Technology. 9 (2020) 16367–16377, https://doi.org/10.1016/J.JMRT.2020.11.102.
[15] H.R. Kotadia, G. Gibbons, A. Das, P.D. Howes, A review of laser powder bed fusion additive manufacturing of aluminium alloys: microstructure and properties, Additive Manufacturing. 46 (2021), 102155, https://doi.org/10.1016/J.ADDMA.2021.102155.
[16] G. Gong, J. Ye, Y. Chi, Z. Zhao, Z. Wang, G. Xia, X. Du, H. Tian, H. Yu, C. Chen, Research status of laser additive manufacturing for metal: a review, Journal of Materials Research and Technology. 15 (2021) 855–884, https://doi.org/10.1016/J.JMRT.2021.08.050.
[17] N. Navin Kumar, A. Chandrakant Yadav, K. Raja, C.D. Naiju, S. Prabhakaran, S. Kalainathan, Laser shock peening on Al-Si10-mg produced by DMLS technique, Materials Today: Proceedings. 22 (2020) 2916–2925, https://doi.org/10.1016/J.MATPR.2020.03.425.
[18] M. Ghasri-Khouzani, X. Li, A.A. Bogno, Z. Chen, J. Liu, H. Henein, A.J. Qureshi, Fabrication of aluminum/stainless steel bimetallic composites through a combination of additive manufacturing and vacuum-assisted melt infiltration casting, J. Manuf. Process. 69 (2021) 320–330, https://doi.org/10.1016/J.JMAPRO.2021.07.047.
[19] A. Riveiro, A. Mejías, F. Lusquiños, J. del Val, R. Comesaña, J. Pardo, J. Pou, Laser cladding of aluminium on AISI 304 stainless steel with high-power diode lasers, Surf. Coat. Technol. 253 (2014) 214–220, https://doi.org/10.1016/J.SURFCOAT.2014.05.039.
[20] J. Yang, J.P. Oliveira, Y. Li, C. Tan, C. Gao, Y. Zhao, Z. Yu, Laser techniques for dissimilar joining of aluminum alloys to steels: a critical review, J. Mater. Process. Technol. 301 (2022), 117443, https://doi.org/10.1016/J.JMATPROTEC.2021.117443.
[21] S.K. Ghosh, K. Bandyopadhyay, P. Saha, Development of an in-situ multi-component reinforced Al-based metal matrix composite by direct metal laser sintering technique — optimization of process parameters, Mater. Charact. 93 (2014) 68–78, https://doi.org/10.1016/J.MATCHAR.2014.03.021.
[22] M. Marrey, E. Malekipour, H. El-Mounayri, E.J. Faierson, A framework for optimizing process parameters in powder bed fusion (PBF) process using artificial neural network (ANN), Procedia Manufacturing. 34 (2019) 505–515, https://doi.org/10.1016/J.PROMFG.2019.06.214.
[23] A. Mostafaei, C. Zhao, Y. He, S. Reza Ghiaasiaan, B. Shi, S. Shao, N. Shamsaei, Z. Wu, N. Kouraytem, T. Sun, J. Pauza, J.V. Gordon, B. Webler, N.D. Parab, M. Asherloo, Q. Guo, L. Chen, A.D. Rollett, Defects and anomalies in powder bed fusion metal additive manufacturing, Curr. Opinion Solid State Mater. Sci. 26 (2022), 100974, https://doi.org/10.1016/J.COSSMS.2021.100974.
[24] B. Haldar, P. Saha, Identifying defects and problems in laser cladding and suggestions of some remedies for the same, Materials Today: Proceedings. 5 (2018) 13090–13101, https://doi.org/10.1016/J.MATPR.2018.02.297.
[25] F. Brückner, D. Lepski, E. Beyer, Modeling the influence of process parameters and additional heat sources on residual stresses in laser cladding, J. Therm. Spray Technol. 16 (3) (2007) 355–373, https://doi.org/10.1007/s11666-007-9026-7.
[26] J. Chen, S. Wang, L. Xue, On the development of microstructures and residual stresses during laser cladding and post-heat treatments, J. Mater. Sci. 47 (2) (2011) 779–792, https://doi.org/10.1007/s10853-011-5854-4.
[27] N. Tamanna, R. Crouch, I.R. Kabir, S. Naher, An analytical model to predict and minimize the residual stress of laser cladding process, Applied Physics A 124 (2) (2018), https://doi.org/10.1007/s00339-018-1585-6.
[28] J. Chen, K. Conlon, L. Xue, R. Rogge, Experimental study of residual stresses in laser clad AISI P20 tool steel on pre-hardened wrought P20 substrate, Mater. Sci.

Eng. A 527 (27–28) (2010) 7265–7273, https://doi.org/10.1016/j.msea.2010.07.098.
[29] J. Tian, P. Xu, Q. Liu, Effects of stress-induced solid phase transformations on residual stress in laser cladding a Fe-Mn-Si-Cr-Ni alloy coating, Mater. Des. 193 (2020), 108824, https://doi.org/10.1016/j.matdes.2020.108824.
[30] A. Calleja, I. Tabernero, A. Fernández, A. Celaya, A. Lamikiz, L.N. López De Lacalle, Improvement of strategies and parameters for multi-axis laser cladding operations, Opt. Lasers Eng. 56 (2014) 113–120, https://doi.org/10.1016/J.OPTLASENG.2013.12.017.
[31] V. Ocelík, M. Eekma, I. Hemmati, J.T.M. de Hosson, Elimination of start/stop defects in laser cladding, Surf. Coat. Technol. 206 (2012) 2403–2409, https://doi.org/10.1016/J.SURFCOAT.2011.10.040.
[32] Y. Zhang, S.S. Babu, C. Prothe, M. Blakely, J. Kwasegroch, M. Laha, G.S. Daehn, Application of high velocity impact welding at varied different length scales, J. Mater. Process. Technol. 211 (2011) 944–952, https://doi.org/10.1016/J.JMATPROTEC.2010.01.001.
[33] V. Gupta, T. Lee, A. Vivek, K.S. Choi, Y. Mao, X. Sun, G. Daehn, A robust process-structure model for predicting the joint interface structure in impact welding, J. Mater. Process. Technol. 264 (2019) 107–118, https://doi.org/10.1016/J.JMATPROTEC.2018.08.047.
[34] A. Kapil, T. Lee, A. Vivek, J. Bockbrader, T. Abke, G. Daehn, Benchmarking strength and fatigue properties of spot impact welds, J. Mater. Process. Technol. 255 (2018) 219–233, https://doi.org/10.1016/J.JMATPROTEC.2017.12.012.
[35] J. Li, B. Schneiderman, S.M. Gilbert, A. Vivek, Z. Yu, G. Daehn, Process characteristics and interfacial microstructure in spot impact welding of titanium to stainless steel, J. Manuf. Process. 50 (2020) 421–429, https://doi.org/10.1016/J.JMAPRO.2019.12.036.
[36] K. Raghukandan, Analysis of the explosive cladding of cu–low carbon steel plates, J. Mater. Process. Technol. 139 (2003) 573–577, https://doi.org/10.1016/S0924-0136(03)00539-9.
[37] S. Mróz, R. Mola, P. Szota, A. Stefanik, Microstructure and properties of 1050A/AZ31 bimetallic bars produced by explosive cladding and subsequent groove rolling process, archives of civil and mechanical, Engineering. 20 (2020) 1–15, https://doi.org/10.1007/S43452-020-00084-4/FIGURES/20.
[38] S.S.H. Inokawa, R. Tomoshige, R. K, Effect of silicon carbide particles in microstructure and mechanical properties of dissimilar aluminium explosive cladding, J. Manuf. Process. 47 (2019) 32–40, https://doi.org/10.1016/J.JMAPRO.2019.09.027.
[39] S. Sadeh, A. Malik, Investigation into the effects of laser shock peening as a post treatment to laser impact welding, Mater. Des. 205 (2021), 109701, https://doi.org/10.1016/J.MATDES.2021.109701.
[40] S. Sunny, G. Gleason, R. Mathews, A. Malik, Simulation of laser impact welding for dissimilar additively manufactured foils considering influence of inhomogeneous microstructure, Mater. Des. 198 (2021), 109372, https://doi.org/10.1016/J.MATDES.2020.109372.
[41] H. Wang, G. Taber, D. Liu, S. Hansen, E. Chowdhury, S. Terry, J.C. Lippold, G. S. Daehn, Laser impact welding: design of apparatus and parametric optimization, J. Manuf. Process. 19 (2015) 118–124, https://doi.org/10.1016/J.JMAPRO.2015.05.007.
[42] H. Wang, K. Wang, W. Zheng, Microstructure complexities of laser impact welded Al-Ti bonding interface, Scr. Mater. 211 (2022), 114488, https://doi.org/10.1016/J.SCRIPTAMAT.2021.114488.
[43] H. Wang, D. Liu, J.C. Lippold, G.S. Daehn, Laser impact welding for joining similar and dissimilar metal combinations with various target configurations, J. Mater. Process. Technol. 278 (2020), 116498, https://doi.org/10.1016/J.JMATPROTEC.2019.116498.
[44] Z. Li, X. Wang, H. Yang, P. Ni, F. Li, H. Liu, Numerical studies on laser impact welding: smooth particle hydrodynamics (SPH), Eulerian, and SPH-Lagrange, J. Manuf. Process. 68 (2021) 43–56, https://doi.org/10.1016/J.JMAPRO.2021.07.021.
[45] H. Liu, H. Jin, M. Shao, H. Tang, X. Wang, Investigation on interface morphology and mechanical properties of three-layer laser impact welding of Cu/Al/Cu, metallurgical and materials transactions a, Physical Metallurgy and Materials Science. 50 (2019) 1273–1282, https://doi.org/10.1007/S11661-018-5074-5/FIGURES/12.
[46] X. Wang, Y. Luo, T. Huang, H. Liu, Experimental investigation on laser impact welding of Fe-based amorphous alloys to crystalline copper, Materials. 10 (2017), https://doi.org/10.3390/MA10050523.
[47] G. Gleason, S. Sunny, R. Mathews, A. Malik, Numerical investigation of the transient interfacial material behavior during laser impact welding, Scr. Mater. 208 (2022), 114325, https://doi.org/10.1016/J.SCRIPTAMAT.2021.114325.
[48] S.Y. Chen, Z.W. Wu, K.X. Liu, X.J. Li, N. Luo, G.X. Lu, Atomic diffusion behavior in cu-Al explosive welding process, J. Appl. Phys. 113 (2013), 044901, https://doi.org/10.1063/1.4775788.
[49] A.M. Rubenchik, J.C. Farmer, L. Hackel, J. Rankin, (2015), Methods and systems for controlled laser-driven explosive bonding, U.S. patent no. 9,192,056 B2, U.S. patent and trademark office.
[50] U.S. Department of Energy News Release, U.S. Department of Energy projects win 36 R&D 100 awards for 2012 technology developments aim to advance American energy, Environment and National Security, June 20, 2012.
[51] Z. Zhang, Y. Zhao, Y. Chen, Z. Su, J. Shan, A. Wu, X. Tang, The role of the pulsed-wave laser characteristics on restraining hot cracking in laser cladding non-weldable nickel-based superalloy, Mater. Des. 198 (2021), 109346, https://doi.org/10.1016/j.matdes.2020.109346.
[52] G. Bidron, A. Doghri, T. Malot, F. Fournier-dit-Chabert, M. Thomas, P. Peyre, Reduction of the hot cracking sensitivity of CM-247lc Superalloy processed by laser cladding using induction preheating, J. Mater. Process. Technol. 277 (2020), 116461, https://doi.org/10.1016/j.jmatprotec.2019.116461.
[53] F. Wang, H. Mao, D. Zhang, X. Zhao, Y. Shen, Online study of cracks during laser cladding process based on acoustic emission technique and finite element analysis, Appl. Surf. Sci. 255 (5) (2008) 3267–3275, https://doi.org/10.1016/j.apsusc.2008.09.039.
[54] Y. Long, P. Nie, Z. Li, J. Huang, X. Li, X. Xu, Segregation of niobium in laser cladding Inconel 718 Superalloy, Trans. Nonferrous Metals Soc. China 26 (2) (2016) 431–436, https://doi.org/10.1016/s1003-6326(16)64131-6.
[55] H. Xie, K. Yang, F. Li, C. Sun, Z. Yu, Investigation on the laves phase formation during laser cladding of IN718 alloy by ca-Fe, J. Manuf. Process. 52 (2020) 132–144, https://doi.org/10.1016/j.jmapro.2020.01.050.
[56] V. Tsigkis, M. Saifur Rahman, L. Hackel, K. Davami, A. Beheshti, A.A. Polycarpou, Helium tribology of Inconel 617 subjected to laser peening for high temperature nuclear reactor applications, Appl. Surf. Sci. 577 (2022), 151961, https://doi.org/10.1016/J.APSUSC.2021.151961.
[57] M. Munther, T. Martin, A. Tajyar, L. Hackel, A. Beheshti, K. Davami, Laser shock peening and its effects on microstructure and properties of additively manufactured metal alloys: a review, Engineering Research Express. 2 (2020), 022001, https://doi.org/10.1088/2631-8695/AB9B16.
[58] T. Palma, M. Munther, M. Sharma, L. Hackel, A. Beheshti, K. Davami, Nanomechanical characterization of laser peened additively manufactured Inconel 718 Superalloy, Adv. Eng. Mater. 21 (2019) 1900499, https://doi.org/10.1002/ADEM.201900499.
[59] L. Hackel, J. Fuhr, M. Sharma, J. Rankin, V. Sherman, K. Davami, Test results for wrought and AM In718 treated by shot peening and laser peening plus thermal microstructure engineering, Procedia Structural Integrity. 19 (2019) 452–462, https://doi.org/10.1016/J.PROSTR.2019.12.049.
[60] A. Tajyar, N. Holtham, N. Brooks, L. Hackel, V. Sherman, A. Beheshti, K. Davami, Laser peening analysis of aluminum 5083: a finite element study, Quantum Beam Science. 5 (2021) 34, https://doi.org/10.3390/QUBS5040034/S1.
[61] X. Wang, M. Shao, H. Jin, H. Tang, H. Liu, Laser impact welding of aluminum to brass, J. Mater. Process. Technol. 269 (2019) 190–199, https://doi.org/10.1016/j.jmatprotec.2019.02.005.
[62] H. Wang, A. Vivek, Y. Wang, G. Taber, G.S. Daehn, Laser impact welding application in joining aluminum to titanium, Journal of Laser Applications. 28 (3) (2016), 032002, https://doi.org/10.2351/1.4946887.
[63] S. Sadeh, A. Malik, Investigation into the effects of laser shock peening as a post treatment to laser impact welding, Mater. Des. 205 (2021), 109701, https://doi.org/10.1016/j.matdes.2021.109701.
[64] T. Lee, S. Zhang, A. Vivek, G. Daehn, B. Kinsey, Wave formation in impact welding: study of the Cu–Ti system, CIRP Ann. 68 (2019) 261–264, https://doi.org/10.1016/J.CIRP.2019.04.058.
[65] A. Szecket, O.T. Inal, D.J. Vigueras, J. Rocco, A wavy versus straight interface in the explosive welding of aluminum to steel, J. Vac. Sci. Technol. A 3 (1998) 2588, https://doi.org/10.1116/1.572839.
[66] D. Jaramillo, A. Szecket, O.T. Inal, On the transition from a waveless to a wavy interface in explosive welding, Mater. Sci. Eng. 91 (1987) 217–222, https://doi.org/10.1016/0025-5416(87)90300-4.
[67] M. Acarer, B. Demir, An investigation of mechanical and metallurgical properties of explosive welded aluminum–dual phase steel, Mater. Lett. 62 (2008) 4158–4160, https://doi.org/10.1016/J.MATLET.2008.05.060.
[68] R.N. Raoelison, D. Racine, Z. Zhang, N. Buiron, D. Marceau, M. Rachik, Magnetic pulse welding: Interface of Al/cu joint and investigation of intermetallic formation effect on the weld features, J. Manuf. Process. 16 (2014) 427–434, https://doi.org/10.1016/J.JMAPRO.2014.05.002.
[69] H. Yu, Z. Xu, Z. Fan, Z. Zhao, C. Li, Mechanical property and microstructure of aluminum alloy-steel tubes joint by magnetic pulse welding, Mater. Sci. Eng. A 561 (2013) 259–265, https://doi.org/10.1016/J.MSEA.2012.11.015.
[70] X. Wu, J. Shang, An investigation of magnetic pulse welding of Al/Cu and interface characterization, journal of manufacturing science and engineering, Transactions of the ASME. 136 (2014), https://doi.org/10.1115/1.4027917/376983.
[71] M. Mandal, S. Patra, R. Chakraborty, P. Saha, M. Shome, Microstructural evolution and nanoindentation study of magnetic pulse welded nitinol and Aluminium sheets, Mater. Charact. 184 (2022), 111690, https://doi.org/10.1016/J.MATCHAR.2021.111690.
[72] T. Sapanathan, R.N. Raoelison, K. Yang, N. Buiron, M. Rachik, Formation of porous inner architecture at the interface of magnetic pulse welded Al/Cu joints, AIP Conference Proceedings. 1769 (2016), 100011, https://doi.org/10.1063/1.4963505.
[73] A. Nassiri, T. Abke, G. Daehn, Investigation of melting phenomena in solid-state welding processes, Scr. Mater. 168 (2019) 61–66, https://doi.org/10.1016/J.SCRIPTAMAT.2019.04.021.
[74] J.R. Rice, D.M. Tracey, On the ductile enlargement of voids in triaxial stress fields*, Journal of the Mechanics and Physics of Solids. 17 (1969) 201–217, https://doi.org/10.1016/0022-5096(69)90033-7.
[75] Y.Z. Bao, Y. Adachi, Y. Toomine, P.G. Xu, T. Suzuki, Y. Tomota, Dynamic recrystallization by rapid heating followed by compression for a 17ni–0.2c martensite steel, Scr. Mater. 53 (12) (2005) 1471–1476, https://doi.org/10.1016/j.scriptamat.2005.08.017.
[76] H.R. Abedi, A. Zarei Hanzaki, Z. Liu, R. Xin, N. Haghdadi, P.D. Hodgson, Continuous dynamic recrystallization in low density steel, Mater. Des. 114 (2017) 55–64, https://doi.org/10.1016/j.matdes.2016.10.044.
[77] J. Humphreys, G.S. Rohrer, A. Rollett, Chapter 11: grain growth following recrystallization, in: Recrystallization and Related Annealing Phenomena, 3rd ed., essay, Elsevier, 2017, pp. 375–429.

[78] F. Grignon, D. Benson, K.S. Vecchio, M.A. Meyers, Explosive welding of aluminum to aluminum: analysis, computations and experiments, International Journal of Impact Engineering. 30 (2004) 1333–1351, https://doi.org/10.1016/J.IJIMPENG.2003.09.049.

[79] Y. Zhang, S.S. Babu, P. Zhang, E.A. Kenik, G.S. Daehn, Microstructure characterisation of magnetic pulse welded AA6061-T6 by electron backscattered diffraction, doi:https://doi.org/10.1179/174329308X341915. 13 (2013) 467–471. doi:https://doi.org/10.1179/174329308X341915.

[80] J. Li, B. Schneiderman, S.M. Gilbert, A. Vivek, Z. Yu, G. Daehn, Process characteristics and interfacial microstructure in spot impact welding of titanium to stainless steel, J. Manuf. Process. 50 (2020) 421–429, https://doi.org/10.1016/j.jmapro.2019.12.036.

[81] T. Lee, A. Nassiri, T. Dittrich, A. Vivek, G. Daehn, Microstructure development in impact welding of a model system, Scr. Mater. 178 (2020) 203–206, https://doi.org/10.1016/j.scriptamat.2019.11.031.

[82] R. Fabbro, J. Fournier, P. Ballard, D. Devaux, J. Virmont, Physical study of laser-produced plasma in confined geometry, J. Appl. Phys. 68 (2) (1990) 775–784, https://doi.org/10.1063/1.346783.

[83] Molecular dynamics (MD) and coarse grain simulation of high strain-rate elastomeric polymers (HSREP), Elastomeric Polymers with High Rate Sensitivity (2015) 187–232, https://doi.org/10.1016/b978-0-323-35400-4.00005-2.